



Cite this: DOI: 10.1039/d3cc02176a

Received 4th May 2023,
Accepted 10th July 2023

DOI: 10.1039/d3cc02176a

rsc.li/chemcomm

An electron acceptor with an intrinsic quinoidal core for bulk-heterojunction organic solar cells and photodetectors†

Haozhe Feng,^{‡a} Bingyan Yin,^{‡a} Langheng Pan,^{‡a} Xinyuan Liu,^{‡a} Seoyoung Kim,^b Yanfei Zhao,^{*c} Xuelong Huang,^{*d} Changduk Yang^{id b} and Chunhui Duan^{id *a}

An electron acceptor based on a quinoidal dipyrrolopyrazinedione core was synthesized for organic solar cells and photodetectors. A power conversion efficiency of 6.7% and a specific detectivity of 4.1×10^{13} Jones at 800 nm have been obtained, suggesting the promising prospects of quinoidal molecules for optoelectronic devices.

Organic solar cells (OSCs) and photodetectors (OPDs) with bulk-heterojunction (BHJ) blends as the photoactive layers have attracted widespread attention owing to their advantages of flexibility, light weight, solution processability, and mass-production ability.^{1–4} Specifically, OSCs have shown great potential in solving the energy shortage and environmental problems.^{1,2} With a similar working principle to OSCs, OPDs exhibited broad applications in medical diagnostics, full colour detection, X-ray imaging, *etc.*^{3,4} The past few years have witnessed the dramatic improvement of OSCs and OPDs. So far, the power conversion efficiencies (PCEs) of OSCs have exceeded 19%,⁵ and OPDs with performance close to silicon photodetectors have been achieved.⁶

One of the key challenges to achieve high performance OSCs and OPDs is to develop advanced electron acceptors with strong near-infrared absorption and excellent electron transport properties.^{7,8} Currently, the electron acceptors have been dominated by A–D–A'–D–A conjugated structures, where A and A'

denote electron-withdrawing units, and D denotes an electron-donating unit. The absorption spectra and energy levels of electron acceptors can be finely tuned by changing the D and A/A' units.^{7,8} The introduction of quinoidal structures is an alternative method to construct high-performance electron acceptors due to a few unique advantages.^{9–13} First, the rigid and coplanar structure of the quinoidal unit is beneficial to the compact π – π stacking and intermolecular charge transport.^{9,10} Second, quinoidal units usually offer excellent delocalization of π -electrons and a strong intramolecular charge-transfer effect, thus leading to narrow optical bandgaps and high absorption coefficients.¹¹ Third, the lactam structures of the quinoidal units can narrow the bandgap by lowering the LUMO energy levels rather than raising the HOMO energy levels,^{12,13} in line with the requirements of stable n-type materials. Our group has reported two quinoidal polymers based on dipyrrolopyrazinedione, which exhibited strong light absorption in the near-infrared region and were used as electron acceptors in all-polymer solar cells.¹⁴ However, research on intrinsic quinoidal molecules for application in OSCs and OPDs still lags behind donor-acceptor type organic semiconductors.

Herein, we report a small molecular electron acceptor PzDP-IC2Cl based on an A–D–Q–D–A type conjugated skeleton and an intrinsic quinoidal dipyrrolopyrazinedione core (Scheme 1). Benefitting from the quinoidal structure and electron-withdrawing nature of dipyrrolopyrazinedione, PzDP-IC2Cl exhibited a light absorption onset over 900 nm and desirable electron acceptor properties. As a result, an OSC with a decent PCE of 6.7% and an OPD with a detectivity up to 4.1×10^{13} Jones at 800 nm have been achieved by PzDP-IC2Cl. To the best of our knowledge, this is the best OSC and the first OPD based on electron acceptors with an intrinsic quinoidal core.

The synthetic route of PzDP-IC2Cl is shown in Scheme 1. Compound 2 was obtained by alkylation starting from compound 1. Compound 3 was then formed *via* a palladium-catalyzed Stille cross-coupling reaction using compound 2 as a starting chemical. Next, compound 4 was converted from

^a Institute of Polymer Optoelectronic Materials and Devices, State Key Laboratory of Luminescent Materials and Devices, South China University of Technology, Guangzhou 510640, China. E-mail: duanchunhui@scut.edu.cn

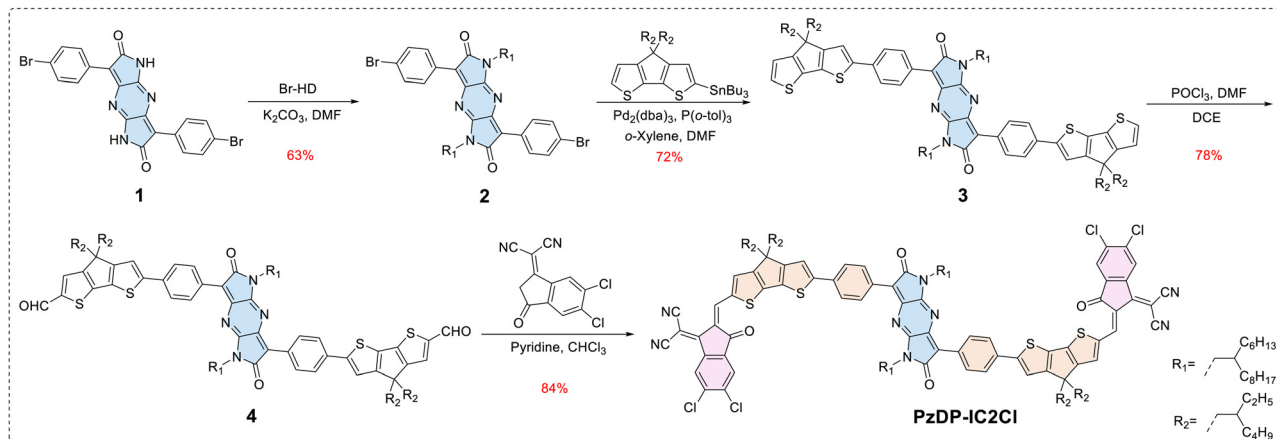
^b School of Energy and Chemical Engineering, Perovtronics Research Center, Low Dimensional Carbon Materials Center, Ulsan National Institute of Science and Technology (UNIST), 50 UNIST-gil, Ulsu-gun, Ulsan 44919, South Korea

^c School of Materials Science and Engineering, Dongguan University of Technology, Dongguan 523808, P. R. China. E-mail: yanfei_zhao0923@163.com

^d Key Laboratory of Prevention and Treatment of Cardiovascular and Cerebrovascular Diseases of Ministry of Education, Gannan Medical University, Ganzhou 341000, P. R. China. E-mail: huangxuelong@gmu.edu.cn

† Electronic supplementary information (ESI) available. See DOI: <https://doi.org/10.1039/d3cc02176a>

‡ These authors contributed equally to this work.



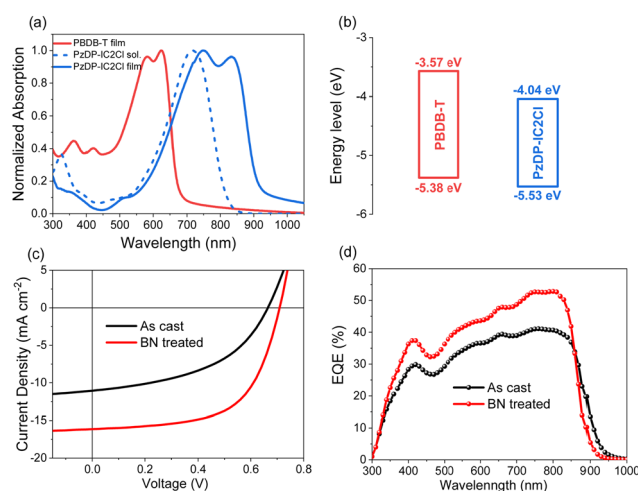
Scheme 1 The chemical structure and synthetic route of PzDP-IC2Cl.

compound 3 by the Vilsmeier–Haack reaction in the presence of phosphorus oxychloride and dry dimethylformamide. Finally, PzDP-IC2Cl was obtained by Knoevenagel condensation between compound 4 and 2-(5,6-dichloro-3-oxo-2,3-dihydro-1H-inden-1-ylidene)malononitrile with a yield of 84%. The chemical structure of PzDP-IC2Cl was fully characterized by ^1H and ^{13}C nuclear magnetic resonance (NMR) and matrix-assisted laser desorption ionization time-of-flight (MALDI-TOF) mass spectroscopy (MS) (Fig. S1–S12, ESI †). PzDP-IC2Cl exhibits good solubility in common organic solvents, such as chloroform and chlorobenzene.

The thermal properties of PzDP-IC2Cl were investigated by thermogravimetric analysis (TGA) and differential scanning calorimetry (DSC). The temperature corresponding to 5% weight loss of PzDP-IC2Cl reached 363 °C (Fig. S13a, ESI †), suggesting good thermal stability of the molecule. In addition, no peaks of melting and crystallization can be observed during the heating and cooling cycle before thermal decomposition of the molecule (Fig. S13b, ESI †).

The normalized absorption spectra of PzDP-IC2Cl in dilute solution and as a thin film are shown in Fig. 1a. The absorption peak of PzDP-IC2Cl was red-shifted from 715 to 837 nm when going from solution to the solid state. The absorption onset of PzDP-IC2Cl is located at 924 nm, corresponding to an optical bandgap of 1.34 eV. The absorption spectrum of PzDP-IC2Cl is complementary to that of PBDB-T (Fig. S14, ESI †), which was selected as the electron donor in OSCs and OPDs in this study. The electrochemical properties of PzDP-IC2Cl were investigated by cyclic voltammetry (CV) (Fig. S15, ESI †). The lowest unoccupied molecular orbital (LUMO) and highest occupied molecular orbital (HOMO) energy levels of PzDP-IC2Cl are -4.04 and -5.53 eV, respectively (Fig. 1b). The energy level offsets between PBDB-T and PzDP-IC2Cl are large enough for efficient charge transfer.

The molecular geometry and electronic structures of PzDP-IC2Cl were investigated by density functional theory (DFT) calculations. The molecule showed good coplanarity with a small dihedral angle of 16.71° between cyclopentadithiophene

Fig. 1 (a) Absorption spectra and (b) energy levels of PBDB-T and PzDP-IC2Cl; (c) J - V curves and (d) EQE spectra of the PzDP-IC2Cl-based OSCs.

and the adjacent phenylene unit (Fig. S16, ESI †), which is conducive to intermolecular π - π stacking and intramolecular charge transfer (ICT). The HOMO is well delocalized along the π -conjugated skeleton, while the LUMO is mainly localized on the electron-withdrawing PzDP unit. The calculated LUMO and HOMO energy levels are -4.19 and -5.78 eV, respectively, agreeing with the results of CV measurements.

The photovoltaic property of PzDP-IC2Cl was investigated in a device of ITO/PEDOT:PSS/active layer/PFN-Br/Ag. The active layer was fully optimized in terms of donor/acceptor weight ratio, thermal annealing, etc. (Table S1, ESI †). The current density–voltage (J - V) characteristics of the OSCs under AM1.5G (100 mW cm^{-2}) irradiation are shown in Fig. 1c, and corresponding parameters are summarized in Table 1. The as-cast device processed from chloroform afforded a PCE of 3.45% with an open-circuit voltage (V_{oc}) of 0.67 V, a short-circuit current density (J_{sc}) of 11.1 mA cm^{-2} , and a fill factor (FF) of 0.470. After introducing 0.5% (v/v) bromonaphthalene (BN) as a solvent additive, the device yielded an improved PCE of 6.70%

Table 1 Photovoltaic parameters of the PzDP-IC2Cl-based OSCs^a

Device	V_{oc} (V)	J_{sc} (mA cm ⁻²)	J_{sc}^b (mA cm ⁻²)	FF (%)	PCE (%)
As cast	0.67 (0.66 ± 0.01)	11.1 (11.0 ± 0.1)	10.9	0.47 (0.46 ± 0.01)	3.50 (3.32 ± 0.08)
BN treated	0.69 (0.69 ± 0.01)	16.1 (15.8 ± 0.3)	15.5	0.60 (0.59 ± 0.03)	6.70 (6.44 ± 0.15)

^a The data in brackets are the average values and standard deviation of at least 12 independent devices for each blend. ^b Obtained from the integration of EQEs with AM1.5G spectrum.

due to boosted J_{sc} (16.1 mA cm⁻²) and FF (0.603). The improvement in J_{sc} has been confirmed by the external quantum efficiencies (EQEs) with less than 5% deviations, as shown in Fig. 1d.

Steady-state photoluminescence (PL) spectra were measured to study the charge transfer behaviors in the OSCs (Fig. S17, ESI†). Both the as-cast and BN treated blend films showed high PL quenching efficiency (ΔPL) when excited at 555 nm, implying efficient electron transfer from donor to acceptor. Upon exciting at 730 nm, the BN treated device showed higher ΔPL (84.2%) than the as-cast device (74.7%), indicating more efficient hole transfer after BN treatment. The photocurrent density (J_{ph}) versus effective voltage (V_{eff}) curves were measured to investigate the exciton dissociation behaviors in the OSCs (Fig. S18, ESI†). The exciton dissociation probabilities (P_{diss}) of the as-cast and BN treated devices were calculated to be 73.1% and 88.2%, respectively, suggesting that BN treatment improved the probability of exciton dissociation in the OSC.

Charge transport properties were measured by the space charge limited current (SCLC) method (Fig. S19, ESI†). The hole mobility (μ_h) and electron mobility (μ_e) of the BN treated device were 1.30×10^{-4} and 9.18×10^{-5} cm² V⁻¹ s⁻¹, respectively, which are higher and more balanced than those of the as-cast device ($\mu_h = 5.26 \times 10^{-5}$, $\mu_e = 2.35 \times 10^{-5}$ cm² V⁻¹ s⁻¹). The results indicated that BN treatment can effectively improve charge transport, which was consistent with the improvement of J_{sc} and FF.

The charge recombination kinetics were investigated by measuring the J_{sc} and V_{oc} under different light intensity (P_{light}). The relationship between J_{sc} and P_{light} can be described as $J_{sc} \propto P_{light}^\alpha$. It is believed that the closer α is to 1, the less bimolecular recombination probability is in the devices.¹⁵ The two OSCs exhibited very close α values (0.967 versus 0.972), which implies negligible bimolecular recombination in these devices (Fig. S20a, ESI†). The plots of $\ln(P_{light})$ and V_{oc} are depicted in Fig. S20b (ESI†), where the slope of the linear section should be nkT/q ($1 < n < 2$), where k is the Boltzmann constant, T is the Kelvin temperature and q is the charge of the primary charge. A larger n indicates more trap-assisted recombination.¹⁵ The n values of the as-cast and BN treated devices were 1.22 and 1.15, respectively. These results suggested that BN treatment reduced the trap-assisted recombination in the OSC, leading to a higher J_{sc} and FF.

The morphology of the blend films was investigated by transmission electron microscopy (TEM). As shown in Fig. S21a (ESI†), the as-cast blend films exhibited distinct agglomeration, which is detrimental to the formation of the bicontinuous interpenetrating network structure. Instead, the morphology of the BN-treated

films was more homogeneous, which is more favorable for efficient exciton dissociation and charge transport in the OSC. We further used two-dimensional grazing incidence wide-angle X-ray scattering (2D-GIWAXS) to investigate the molecular packing and orientation in the two films, as shown in Fig. S21b (ESI†). The corresponding numerical data are summarized in Tables S2 and S3 (ESI†). The PzDP-IC2Cl neat film showed a strong (100) peak at $q = 0.36 \text{ \AA}^{-1}$ in the out-of-plane (OOP) direction and a strong (010) peak at $q = 1.80 \text{ \AA}^{-1}$ in the in-plane (IP) direction, indicating a predominant edge-on orientation. For the as-cast blend film, the IP (010) and OOP (100) diffraction peaks of PzDP-IC2Cl as well as the OOP (010) and IP (100) diffraction peaks of PBDB-T were maintained, implying that the molecular orientation and stacking ordering of the donor and acceptor were not disrupted upon blending. After BN treatment, the diffraction peaks at $q = 0.29$ and $q = 0.40 \text{ \AA}^{-1}$ in the IP direction emerged, while the IP (010) diffraction peak at $q = 1.80 \text{ \AA}^{-1}$ disappeared. These results

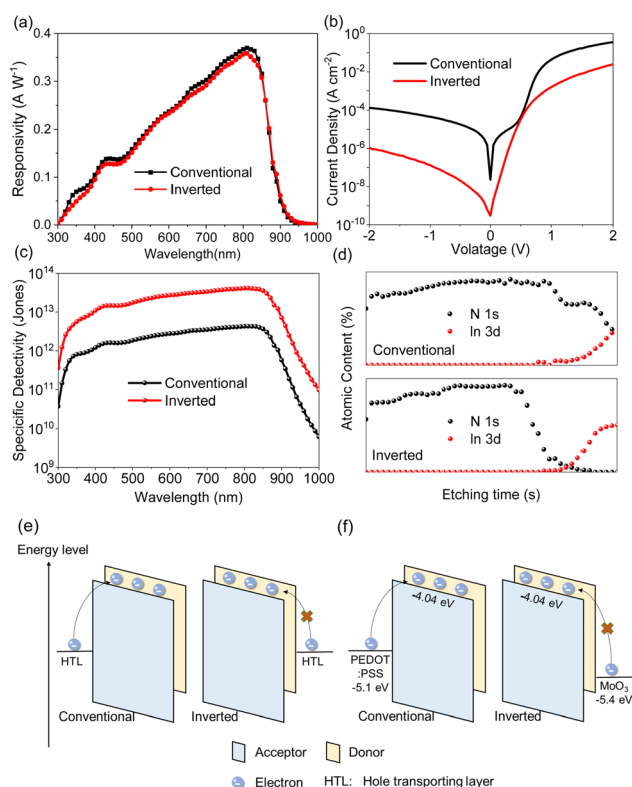


Fig. 2 (a) Responsivities, (b) dark current densities, and (c) detectivities of the OPDs based on PzDP-IC2Cl. (d) XPS depth profiles of the blends. (e and f) Schematic diagrams of the dark current injection mechanism from vertical distributions (e) and interface work functions (f).

Table 2 Parameters of the PzDP-IC2Cl-based OPDs at 800 nm under 0 V bias^a

Device	EQE (%)	R (A W^{-1})	J_d at 0 V (A cm^{-2})	D^* (Jones)
Conventional	56.9 (56.6 ± 0.3)	0.37 (0.36 ± 0.07)	2.30×10^{-8} (2.33 ± 0.03)	4.28×10^{12} (4.16 ± 0.12)
Inverted	55.2 (54.8 ± 0.4)	0.36 (0.35 ± 0.06)	2.33×10^{-10} (2.35 ± 0.02)	4.12×10^{13} (4.03 ± 0.09)

^a The data in brackets are the average values and standard deviation of at least 8 independent devices for each device structure.

suggested the suppressed edge-on orientation and enhanced face-on orientation of PzDP-IC2Cl. The maintained ordering and face-on orientation were beneficial to charge transport, which supports the higher J_{sc} and FF.

Inspired by the decent EQE of the PzDP-IC2Cl-based OSC in the near-infrared region (Fig. 1d), we further explored the potential of a quinoidal molecule in OPDs. Generally, a vertical composition distribution in the active layer and the work function of the interlayer have significant impacts on the performance of OPDs.¹⁶ Therefore, the OPD performance of PzDP-IC2Cl was evaluated in both conventional and inverted devices (Fig. S22, ESI†). The EQE spectra and responsivities (R) of the OPDs with different device structures were almost the same (Fig. S23, ESI† and Fig. 2a). However, the dark current density (J_d) of the inverted device was about two orders of magnitude lower than that of the conventional device (Fig. 2b), resulting in a much higher detectivity (D^*) of 4.12×10^{13} Jones at 800 nm under 0 V bias (Fig. 2c). The numerical parameters of the OPDs are summarized in Table 2.

It is widely known that J_d is closely related to charge injection. A vertical composition distribution in the active layer may have a significant impact on the J_d of OPDs. A vertical composition distribution with the donor enriched at the anode side and acceptor enriched at the cathode side is more favorable to block the undesirable charge injection (Fig. 2e). Therefore, X-ray photoelectron spectroscopy (XPS) was used to elucidate the differences of J_d in OPDs. We chose nitrogen as the characteristic element of PzDP-IC2Cl. As shown in Fig. 2d, the content of nitrogen increased with the etching time, indicating an increased PzDP-IC2Cl content in the bottom of the active layer. Obviously, the vertical distribution of PzDP-IC2Cl was more likely to block the undesirable charge injection in the inverted structure, which led to a lower J_d . In addition, the energy level is also connected to the interface energy barrier. The work function of MoO_3 (-5.4 eV) is considerably deeper than that of PEDOT:PSS (-5.1 eV), which built a larger energy barrier for undesirable electron injection from anode contact (Fig. 2f) and contributed to the lower J_d .

In summary, a novel small molecular acceptor PzDP-IC2Cl with near-infrared light absorption and appropriate energy levels based on an intrinsic quinoidal core was developed. By blending with PBDB-T in OSCs, a record-high efficiency among small molecular acceptors with an intrinsic quinoidal core was realized by PzDP-IC2Cl. The newly developed quinoidal

acceptor was also applied in OPDs for the first time and a detectivity up to 4.1×10^{13} Jones at 800 nm under 0 V bias was obtained. Overall, this work demonstrated the promising potential of quinoidal molecules in bulk-heterojunction organic optoelectronic devices.

The research was financially supported by the National Natural Science Foundation of China (22275058 and U20A6002), Guangdong Basic and Applied Basic Research Foundation (2022B1515120008), and Guangdong Innovative and Entrepreneurial Research Team Program (2019ZT08L075). C. Y. acknowledges the National Research Foundation of Korea (NRF) grant funded by the Korea government (MSIP) (2021R742C3004202).

Conflicts of interest

There are no conflicts to declare.

Notes and references

- G. Zhang, F. R. Lin, F. Qi, T. Heumüller, A. Distler, H.-J. Egelhaaf, N. Li, P. C. Y. Chow, C. J. Brabec, A. K. Y. Jen and H.-L. Yip, *Chem. Rev.*, 2022, **122**, 14180.
- J. S. Park, G.-U. Kim, S. Lee, J.-W. Lee, S. Li, J.-Y. Lee and B. J. Kim, *Adv. Mater.*, 2022, **34**, 2201623.
- J. Liu, M. Gao, J. Kim, Z. Zhou, D. S. Chung, H. Yin and L. Ye, *Mater. Today*, 2021, **51**, 475.
- H. Ren, J. D. Chen, Y. Q. Li and J. X. Tang, *Adv. Sci.*, 2021, **8**, 2002418.
- L. Zhu, M. Zhang, J. Xu, C. Li, J. Yan, G. Zhou, W. Zhong, T. Hao, J. Song, X. Xue, Z. Zhou, R. Zeng, H. Zhu, C.-C. Chen, R. C. I. MacKenzie, Y. Zou, J. Nelson, Y. Zhang, Y. Sun and F. Liu, *Nat. Mater.*, 2022, **21**, 656.
- Y. Song, Z. Zhong, P. He, G. Yu, Q. Xue, L. Lan and F. Huang, *Adv. Mater.*, 2022, **34**, 2201827.
- B. Xie, Z. Chen, L. Ying, F. Huang and Y. Cao, *InfoMat*, 2020, **2**, 57.
- D. Meng, R. Zheng, Y. Zhao, E. Zhang, L. Dou and Y. Yang, *Adv. Mater.*, 2022, **34**, 2107330.
- M. Yang, T. Du, X. Zhao, X. Huang, L. Pan, S. Pang, H. Tang, Z. Peng, L. Ye, Y. Deng, M. Sun, C. Duan, F. Huang and Y. Cao, *Sci. China: Chem.*, 2021, **64**, 1219.
- T. Mikie and I. Osaka, *J. Mater. Chem. C*, 2020, **8**, 14262.
- K. Kawabata and K. Takimiya, *Chem. – Eur. J.*, 2021, **27**, 15559.
- C. Zhang and X. Zhu, *Adv. Funct. Mater.*, 2020, **30**, 2000765.
- T. Du, Y. Liu, Y. Deng and Y. Geng, *Chin. J. Chem.*, 2023, **41**, 776.
- L. Pan, T. Zhan, J. Oh, Y. Zhang, H. Tang, M. Yang, M. Li, C. Yang, X. Liu, P. Cai, C. Duan, F. Huang and Y. Cao, *Chem. – Eur. J.*, 2021, **27**, 13527.
- M. M. Mandoc, F. B. Kooistra, J. C. Hummelen, B. de Boer and P. W. M. Blom, *Appl. Phys. Lett.*, 2007, **91**, 263505.
- W. Jang, B. G. Kim, S. Seo, A. Shawky, M. S. Kim, K. Kim, B. Mikkladal, E. I. Kauppinen, S. Maruyama, I. Jeon and D. H. Wang, *Nano Today*, 2021, **37**, 101081.